Magnesium inhibition of calcite dissolution kinetics

Rolf S. Arvidson [a,*], Martin Collier [a], Kevin J. Davis [a], Michael D. Vinson [a],
James E. Amonette [b,c], Andreas Luttge [a,d]

[a] Department of Earth Science MS-126, Rice University, P.O. Box 1892, Houston, TX 77251-1892, USA
[b] Environmental Molecular Sciences Laboratory, Richland, WA 99352, USA
[c] Pacific Northwest National Laboratory, Richland, WA 99352, USA
[d] Department of Chemistry, Center for Biological and Environmental Nanotechnology (CBEN), Rice University,
P.O. Box 1892, Houston, TX 77251-1892, USA

Abstract

We present evidence of inhibition of calcite dissolution by dissolved magnesium through direct observations of the (104) surface using atomic force microscopy (AFM) and vertical scanning interferometry (VSI). Far from equilibrium, the pattern of magnesium inhibition is dependent on solution composition and specific to surface step geometry. In CO_2-free solutions (pH 8.8), dissolved magnesium brings about little inhibition even at concentrations of 0.8×10^{-3} molal. At the same pH, magnesium concentrations of less than 0.05×10^{-3} molal in carbonate-buffered solutions generate significant inhibition, although no changes in surface and etch pit morphology are observed. As concentrations exceed magnesite saturation, the dissolution rate shows little additional decrease; however, selective pinning of step edges results in unique etch pit profiles, seen in both AFM and VSI datasets. Despite the decreases in step velocity, magnesium addition in carbonated solutions also appears to activate the surface by increasing the nucleation rate of new defects. These relationships suggest that the modest depression of the bulk rate measured by VSI reflects a balance between competing reaction mechanisms that simultaneously depress the rate through selective inhibition of step movement, but also enhance reactivity on terraces by lowering the energy barrier to new etch pit formation.
© 2005 Elsevier Inc. All rights reserved.

1. Introduction

Magnesium dissolved in natural waters is one of the most important components to interact with the calcite surface, and the thermodynamics and kinetics of this interaction have long been a focus of studies in carbonate geochemistry (e.g., Berner, 1967, 1975). Much of the current focus involves understanding the role of magnesium during biomineralization through direct, in situ observations of reacting calcite surfaces. Recent AFM work has shown how increasing magnesium brings about reductions in step velocity and changes in step morphology (Davis et al., 2000, 2001, 2004; Wasylenki et al., 2004). These changes are thought to reflect increased solubility from lattice uptake of magnesium, thus reducing the driving force for growth at screw dislocations. However, this mechanism cannot explain the magnesium inhibition of the *dissolution* reaction, which by comparison has received less attention. Although it is generally accepted that Mg inhibition of dissolution reflects sorption at specific surface sites, this process is not understood in any detail. Our purpose in this paper is to present direct observations and quantification of this inhibition on the calcite surface. In an integrated approach, we have used vertical scanning interferometry (VSI) to measure the dissolution rate as a function of magnesium concentration over tens to hundreds of hours, complemented with atomic force microscopy (AFM) fluid cell experiments to provide details of specific step movement over shorter time periods. This work is an extension of that presented in Arvidson et al. (2003a), in which we applied

* Corresponding author. Fax: +1 713 348 5214.
  E-mail address: rsa4046@ruf.rice.edu (R.S. Arvidson).

VSI to the study of calcite dissolution in simple carbonated solutions. With few exceptions, the base NaHCO$_3$/Na$_2$CO$_3$ solution (prior to Mg addition) used in the experiments presented here was prepared identically to that of the previous work.

Only a relatively small number of papers from the voluminous literature on calcite dissolution report explicit measurement of magnesium inhibition. In this paper we have excluded reference to work in diffusion-controlled (e.g., Buhmann and Dreybrodt, 1987) or quasi-equilibrium regimes, as well as in seawater, where the variation in the dissolution rate is primarily a complex function of the distance from equilibrium (Berner and Morse, 1974; Morse, 1974). As used below, the distance from equilibrium is defined as the free energy (ΔG_r) for the overall dissolution reaction CaCO$_{3(calcite)}$ = Ca$^{2+}_{(aq)}$ + CO$_3^{2-}_{(aq)}$, such that exp(ΔG_r/RT) = $(\prod a_i^{v_i})/K$, where a_i are the activities computed from free ion concentrations and single ion activity coefficients, v_i are the stoichiometric coefficients for the reaction as written, K is the thermodynamic equilibrium constant, and the solid is assumed to be pure calcite having unit activity.

Sjöberg (1978) fitted calcite dissolution rate data (5–60 × 10^{-3} molar Mg^{2+}, pH 8.3) to a Langmuir adsorption isotherm

$$1 - R/R_0 = a[Mg^{2+}]/(1 + b[Mg^{2+}]) \qquad (1)$$

having empirical parameters $a = 1.38 \times 10^2$ and $b = 1.68 \times 10^2$, and observed that magnesium's effectiveness as an inhibitor increased as equilibrium was approached. In the presence of both calcium and magnesium ions, he speculated that their competitive adsorption led to development of a Ca–Mg surface phase consistent with an ion exchange equilibrium. Compton and Brown (1994) observed a ~50% rate reduction at MgSO$_4$ = 40 × 10^{-3} molar (pH 8–9, pCO$_2$ ~ 0). Alkattan et al. (2002) observed no inhibition at higher concentrations (100 × 10^{-3} molal MgCl$_2$) but very low pH (1–3). Closer to equilibrium ($\Delta G_r = -0.7$ kJ/mol), Gutjahr et al. (1996) found magnesium to have no effect on dissolution rate at Mg(NO$_3$)$_2 \leqslant 0.3 \times 10^{-3}$ molal. This last result is inconsistent with the work of Sabbides and Koutsoukos (1995), who observed a threefold reduction in rate using synthesized calcite seed crystals at $-\Delta G_r = 0.3 \sim 0.2$ kJ/mol and Mg^{2+} = 40 × 10^{-6} molar. Thus, although it is clear that magnesium suppresses dissolution under certain conditions, the diversity in experimental regimes makes it difficult to draw precise conclusions regarding its inhibitor role versus that of other components. Although it is frequently assumed that magnesium's interaction with the calcite surface behaves according to a Langmuir adsorption isotherm, it is also unclear whether true reversibility can be demonstrated, and furthermore this conclusion contains no mechanistic insight. One means of gaining this insight is through direct observation of step motion on the surface.

The oblique intersection of the (104) cleavage surface with its c-axis creates monomolecular (0.3 nm) step edge faces that lie at obtuse and acute angles to the surface (nominally 102° and 78°, respectively). These step edges are present in symmetrically equivalent orientations ($\langle 48\bar{1}\rangle$, $\langle \bar{4}41\rangle$, Paquette and Reeder, 1995). For clarity and consistency, obtuse and acute steps in this paper will be denoted by "o" and "a" subscripts, respectively, instead of the signed (+, −) notation found elsewhere in the literature. AFM step velocities are generally higher for obtuse compared with acute steps during growth and dissolution (Gratz et al., 1993; Liang and Baer, 1997), although this relationship is sensitive to the distance from equilibrium (e.g., Teng et al., 1999), Ca^{2+}/CO$_3^{2-}$ activity ratio (Arvidson et al., 2003b) and impurity burden (Teng et al., 1998; Davis et al., 2000). Velocity differences may reflect the orientation of trigonal carbonate groups at obtuse versus acute step edges: leading "out-of-plane" oxygen atoms reside above the upper cleavage surface at acute steps and below at obtuse steps. In addition to direct AFM observations, calcite molecular dynamics simulations also show preferential dissolution on obtuse versus acute stepped surfaces (de Leeuw and Parker, 1999), and preferential uptake of Mg^{2+} (versus growth of pure CaCO$_3$) on calcite step edges (de Leeuw, 2002).

2. Methods

We measured magnesium inhibition of calcite dissolution on single crystal (104) surfaces by two complementary approaches:

1. A single calcite cleavage rhomb mounted within a fluid cell was reacted with a flowing solution of fixed composition for discrete time intervals. The changes in surface topography of the mineral were recorded by vertical scanning interferometry (VSI). This method, described in detail in Arvidson et al. (2003a), allows quantitative mapping of relatively large areas of the mineral surface (~0.5 mm^2 field of view using a 10 × objective) at subnanometer vertical resolution, and obtains absolute surface-normal retreat rates.
2. Step velocities were measured using similarly prepared calcite surfaces with flowing reactant solutions in an AFM fluid cell (Digital Instruments Nanoscope III Multimode SPM operated in contact mode). Scanning frequencies were typically 12 Hz, with scan areas ranging between 5 × 5 and 30 × 30 μm. This approach is also described in detail in Davis et al. (2000).

The flow cells and flow rates used in these experiments are similar to those of previous VSI (Arvidson et al., 2003a) and AFM (Davis et al., 2000) experiments. We did not attempt to establish hydrodynamic descriptions of these flow environments (e.g., Coles et al., 1998; Higgins et al., 2002), and have instead employed sufficiently high flow rates to measure dissolution rates that reflect surface control. This strategy is consistent with many of the published AFM experiments that address both calcite dissolu-

tion (Liang et al., 1996; Liang and Baer, 1997) and growth (e.g., Teng et al., 1998). In our VSI work, the nominal volume (i.e., before the sample crystal is mounted) of the flow cell is 350 μL. This wetted volume is reduced by a factor of at least two by the addition of the single crystal during the experiment. The flow rate for all experiments was maintained at 85 μL/s, giving a maximum computed residence time of ~2 s. Although providing no insight into flow regime hydrodynamics, this residence time is below that indicated for the onset of diffusively limited step velocities (cf. 2.5 μL/s flow rate, ~20 μL reaction volume, Liang et al., 1996; Liang and Baer, 1997). In previous VSI experiments (Arvidson et al., 2003a), we have also found that increases in flow rate using this cell brought about *no* increase in dissolution rate (within error). We are thus confident that both our AFM and VSI measurements represent only surface-controlled reactions, and are independent of flow regime and cell geometry.

All experiments used cleavage rhombs derived from synthetic calcite (Commercial Crystal Laboratories, Naples FL) tested for compositional (Varian Vista Pro ICP-AES) and mineralogical (Rigaku DMAX 2000) purity. Standard reactant solutions were prepared from 18.2 MΩ-cm water and high purity reagent $NaHCO_3$ (total alkalinity 4.4×10^{-3} eq/kg-H_2O). These were continuously equilibrated with atmospheric CO_2 (pH 8.80 ± 0.03 at 25 °C, measured by combination glass electrode; cf. Liang et al., 1996; Lea et al., 2001). Mg was added as $MgCl_2$ to give concentrations of 0.01×10^{-3}, 0.05×10^{-3}, 0.3×10^{-3}, and 0.8×10^{-3} molal. The lower and upper limit of concentrations were chosen on the basis of detection limits and the desire to avoid nucleation of magnesian phases (brucite, magnesite). The effect of dissolved inorganic carbon was evaluated in additional experiments at 0.8×10^{-3} molal $MgCl_2$ by excluding CO_2 through continuous sparging with high purity N_2, pH adjustment with NaOH, and ionic strength adjustment by NaCl addition. In the text, we shall often refer to the $NaHCO_3$-buffered solutions as "carbonated" to distinguish them from their CO_2-free counterparts.

Total dissolved magnesium was measured by colorimetric EDTA titration (for concentrations greater than 0.1×10^{-3} molal, 0.3% precision) or by nitrous flame AA (2% precision). Total chloride was determined by potentiometric titration with $AgNO_3$ (0.3% precision). Total sodium was generally not measured but computed by charge balance from alkalinity and chloride concentrations. Input solutions were Ca^{2+}-free. Calcium concentrations of reacted solutions were also not measured directly, but instead computed on the basis of the rate measured by VSI (see below) applied to the total surface area of the wetted crystal surface. Solution (total) alkalinity was measured by high precision potentiometric Gran titration with HCl (0.1% precision) but no differences in total alkalinity between input and reacted solutions could be found. The equilibrium concentrations and activity of dissolved species (e.g., Fig. 1D) were computed from measured pH, total alkalin-

ity, and total dissolved components using an ion-association model (Arvidson and Mackenzie, 1999), and calculations using this model confirmed far-from-equilibrium conditions with respect to calcite (Ca^{2+}_T between 4 and 0.4 nM, with ΔG_r between −23 and −28 kJ/mol). Experimental conditions are given in Table 1.

As dissolution proceeds, etch pits typically form on the calcite surface, decreasing the mean height of the original surface. Reaction rates were computed from the VSI data by measuring the decrease in the mean height of the surface as a function of time. These height data were compared with those of an area of the sample surface protected by an inert polymer applied as a mask, which thus provided an unreacted reference surface (for a complete description of these techniques, see Luttge et al., 1999, 2003; Arvidson et al., 2003a). From the AFM experiments, step velocity data were collected by measuring the distance over which a monomolecular step edge traversed between individual (deflection) scan images, with the crystal oriented such that one step direction was perpendicular to the scan axis. Step velocity measurements were always made from images scanned in the same direction. This technique assumes that there is no significant physical drift between scans, a condition we verified by evaluating the consistency of velocities recorded under the same conditions, and by observation of "fixed" landmarks on the mineral surface.

3. Results

3.1. VSI experiments

VSI results are summarized in Table 2, Figs. 1 and 2. In carbonated solutions at pH 8.8, we observed that the VSI rate varied from $0.23 \pm 0.01 \times 10^{-7}$ mol/m²/s (Run V2C, no Mg) to $0.02 \pm 0.02 \times 10^{-7}$ mol/m²/s (Run V6C, 0.8×10^{-3} molal Mg). Fig. 1B shows that most of the decrease in rate occurs at relatively low Mg concentrations, i.e., less than 0.1×10^{-3} molal, close to the region of approximate magnesite saturation (the thermodynamic constant for magnesite is computed from SUPRCT92, Johnson et al., 1992). As magnesium concentrations increase beyond this point, little additional inhibition is observed and rates at 0.3 and 0.8×10^{-3} molal Mg are identical within the error of the measurements. However, this inhibition is *not* accompanied by any reduction in etch pit nucleation. Long term VSI experiments clearly show that new pits continue to nucleate on the surface even at 0.8×10^{-3} molal Mg, and our AFM data indicate that the etch pit nucleation rate responds rapidly and *positively* to Mg introduction. To compare with the results of Sjöberg (1978), we fitted our data to a Langmuir adsorption isotherm (see Eq. (1) and Fig. 1B). The parameters from this fit ($a = 6.1 \times 10^4$, $b = 6.5 \times 10^4$, using the same units) are substantially larger than those found by Sjöberg (1978) and suggest that the effectiveness of Mg as an inhibitor is increased under the conditions of our experiments.
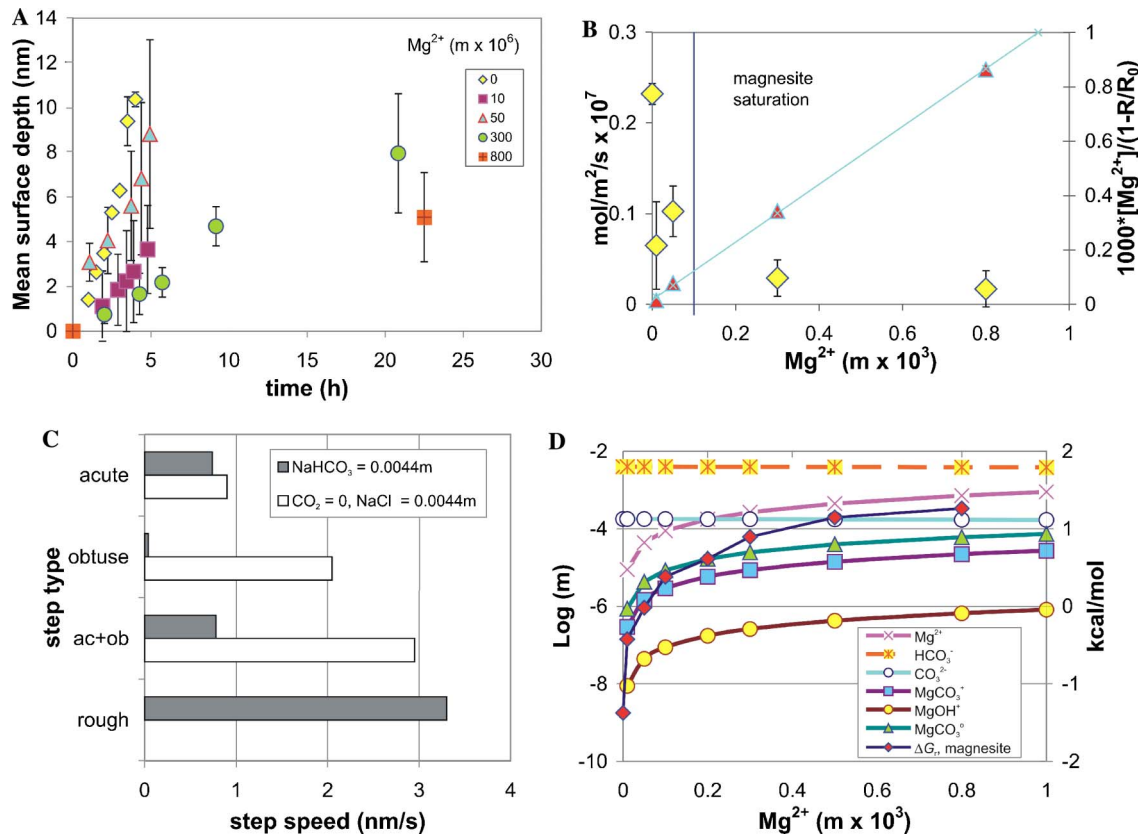
Fig. 1. Experimental results from VSI and AFM runs. (A) Change in mean surface height (expressed here as depth) of (104) surface measured by VSI as a function of time from runs V2C through V6C, plotted for different $MgCl_2$ concentrations (diamond, 0; solid square, 0.01; triangle, 0.05; circle, 0.3; and crossed square, 0.8×10^{-3} molal), in 4.4×10^{-3} molal $NaHCO_3$, atmospheric pCO_2, pH 8.8. Error bars reflect repeat determinations from the same reacted surface. Absolute rates are not available for runs V1C and V7N rates because of mask failure. (B) Combined plot of specific dissolution rate computed from velocity data (LH axis, diamonds) and Langmuir adsorption plot (RH axis, triangles). Vertical line is computed magnesite equilibrium. The error bars reflect primarily variations in etch pit density (e.g., Blum and Lasaga, 1990; MacInnis and Brantley, 1993). (C) AFM step velocities compared at constant $[Mg^{2+}] = 0.8 \times 10^{-3}$ molal in carbonated (closed bars, 4.4×10^{-3} molal $NaHCO_3$, AFM Run A4C) versus CO_2-free (open bars, 4.4×10^{-3} molal NaCl, AFM Run A5N) solutions, measured at acute versus obtuse steps; "ac + ob" are summed velocities. "Rough" steps are discussed in text. (D) Distribution of dissolved species in the standard solution (4.4×10^{-3} molal $NaHCO_3$) as a function of magnesium concentration; ΔG_r for magnesite shown for comparison.

Table 1
Experimental conditions

	N time steps	Total t (h)	pH	T (°C)	Total alkalinity (eq/kg × 10³)	MgCl₂ (molal × 10³)	NaCl (molal × 10³)
VSI Runs							
V1C	1	172	8.80	21.0	4.40	—	—
V2C	7	24.0	8.81	24.0	4.40	—	—
V3C	5	20.9	8.77	22.4	4.40	0.01	—
V4C	5	4.93	8.76	21.4	4.40	0.05	—
V5C	5	20.8	8.76	22.9	4.40	0.30	—
V6C	1	22.5	8.71	21.0	4.40	0.80	—
V7N	1	24.0	8.80	22.0	0.0012	0.80	4.40
AFM Runs							
See Table 1 of Vinson and Luttge (2005)			8.8	22.0	4.40	—	—
A4C			8.80	22.0	4.40	0.80	—
A3N			8.80	22.0	0.0012	0.80	4.40
A5N			11.0	22.0	1.2	0.80	4.40

In VSI run V7N and AFM runs A3N and A5N, CO_2 was excluded by continuously sparging with high purity N_2, and total Na and pH were adjusted by NaCl and NaOH addition, respectively. In all other runs, alkalinity was fixed with $NaHCO_3$ and pCO_2 was maintained at an approximately constant value by continuous sparging with laboratory air. Also note that AFM run A4C alternated Mg concentration between 0 and 0.8×10^{-3} molal at constant alkalinity (see text and Figs. 3 and 4).

Table 2
VSI surface normal dissolution rates and AFM step velocities

VSI Runs	Rate (mols/m²/s × 10⁷)		
V1C	—		
V2C	0.23 ± 0.01		
V3C	0.07 ± 0.05		
V4C	0.10 ± 0.03		
V5C	0.03 ± 0.02		
V6C	0.02 ± 0.02		
V7N	—		
AFM Runs	**Step velocities (nm/s)**		
	Acute (v_a)	Obtuse (v_o)	$v_o + v_a$	v_o/v_a
Vinson and Luttge (2005) (zero Mg datum)	1.14	1.1	1.37	1.31
A4C (0.8×10^{-3} molal Mg)	0.74 ± 0.07	0.04 ± 0.03	0.78 ± 0.08	0.05 ± 0.04
A3N	0.90 ± 0.09	2.05 ± 0.05	2.95 ± 0.10	2.3 ± 0.2
A5N	0.35 ± 0.02	1.68 ± 0.09	2.03 ± 0.09	4.8 ± 0.4

Subscripts o and a refer to obtuse and acute steps, respectively.

At magnesium concentrations equal to or less than 0.05×10^{-3} molal, etch pit development followed a consistent pattern. After their initial appearance on the surface, etch pits would increase in diameter at a constant rate, until coalescence with neighboring pits. However, most pits did not steadily increase in depth, and reduction in the rate of deepening resulted in flat-bottomed, steep-sided profiles. After variable increase in the diameter of a flat-bottomed pit, new pits would nucleate within the interior floor, and deepening would begin anew. This process produced a variation in the profiles of etch pit walls, and many "mature" pits exhibited a flat-bottomed interior floor bounded by steeply sloping, but commonly "stair-stepped" sides (Fig. 2A). These observations are also consistent with numerous AFM calcite dissolution experiments (e.g., Liang et al., 1996).

Our most striking observation is the change in etch pit morphology at higher Mg concentrations. At 0.05×10^{-3} molal Mg and below, etch pits at any point in time maintained a symmetric rhombic outline. We observed variable minor pinning at the vertex of the $\langle 48\bar{1} \rangle_o$, $\langle \bar{4}41 \rangle_o$ step edges (arrow, Fig. 2A). Previous AFM and VSI studies have shown that etch pits developing in carbonated (Mg-free) solutions (pH 8.8) develop rounding at the intersection of the obtuse step edges (cf. AFM data of Lea et al., 2001, VSI data of Arvidson et al., 2003a). Lea et al. (2001) attributed this result to the action of dissolved carbonate or bicarbonate species and a reduction in the velocity of the obtuse steps, whose nominal velocity in pure water is 1.5–2.3 times that of the acute steps.

With increasing Mg concentrations ($>0.05 \times 10^{-3}$ molal), we observed that etch pit morphology progressively departed from the characteristic rhombic symmetry. First, the minor rounding of obtuse–obtuse (o, o) intersections disappeared, and these corners were instead sharp and well defined. Second, comparison of time-lapse sequences using
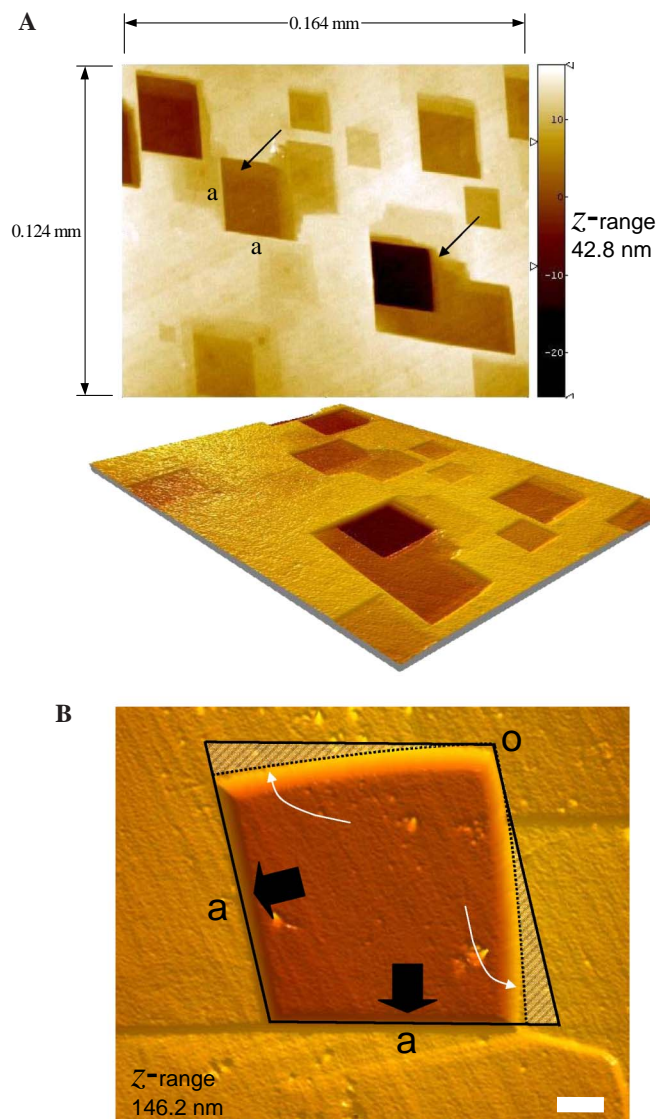

Fig. 2. Mg influence on etch pit morphology, VSI. (A) 2D and 3D view of etch pits developing on calcite surface at 0.01×10^{-3} molal Mg. Black arrows point to slight pinning of obtuse steps comprising etch pit margins. (B) Etch pit formed in 0.8×10^{-3} molar Mg by motion (large black arrows) of acute steps ("a") only; obtuse steps are completely pinned. Triangular regions with diagonal hatching show the difference between an ideal rhombohedral symmetry (solid black outline) and the *actual* etch pit boundary (dotted lines at *white* arrows are the obtuse step edges). The hatched regions thus represent the volume of undissolved material that is not removed due to incomplete migration of obtuse-facing kinks along the acute step edge. Scale bar 10 µm.

pixel registration of a fixed reference point showed severe obtuse step pinning along the entire length of the step, resulting in no detectable movement. The expansion of etch pits thus reflected migration of acute steps only. In addition, the movement of acute steps produced obtuse step edges that curved toward the (o, a) intersection. Fig. 2B shows this development: the thin, triangular, hatched areas represent the difference between the actual obtuse step traces and ideal ones symmetrical to their acute counterparts. This pattern was highly reproducible as a function of time,

and pits growing for over 24 h maintained this asymmetric outline.

3.2. AFM experiments

We compared our observations of dissolution rate, inhibition, and etch pit morphologies made with the interferometer to those achieved at higher resolution with the AFM. Here the ability to rapidly exchange solutions in the flow cell allowed us to immediately assess the dissolving surface's response to the appearance of inhibitor species. In AFM Run A4C, we exchanged our "standard" Mg-free solution (4.4×10^{-3} molal $NaHCO_3$, pH 8.8) with a solution having 0.8×10^{-3} molal Mg at the same pH

and carbonate alkalinity (Table 1; the step velocity data for this standard solution are taken from work already published by Vinson and Luttge (2005), but were acquired during the same experimental session). Fig. 3 shows a sequence in which a previously developed etch pit, grown in carbonated Mg-free solution, is the site of new etch pit formation once Mg is introduced. This sequence confirms our previous VSI observations that (1) the obtuse steps are severely inhibited after Mg introduction and do not measurably advance, and thus (2) subsequent etch pit growth occurs almost entirely by the advance of acute steps.

Although we observed some pinning of obtuse steps in Mg-free standard solution (see Figs.4B1–B3), net move-
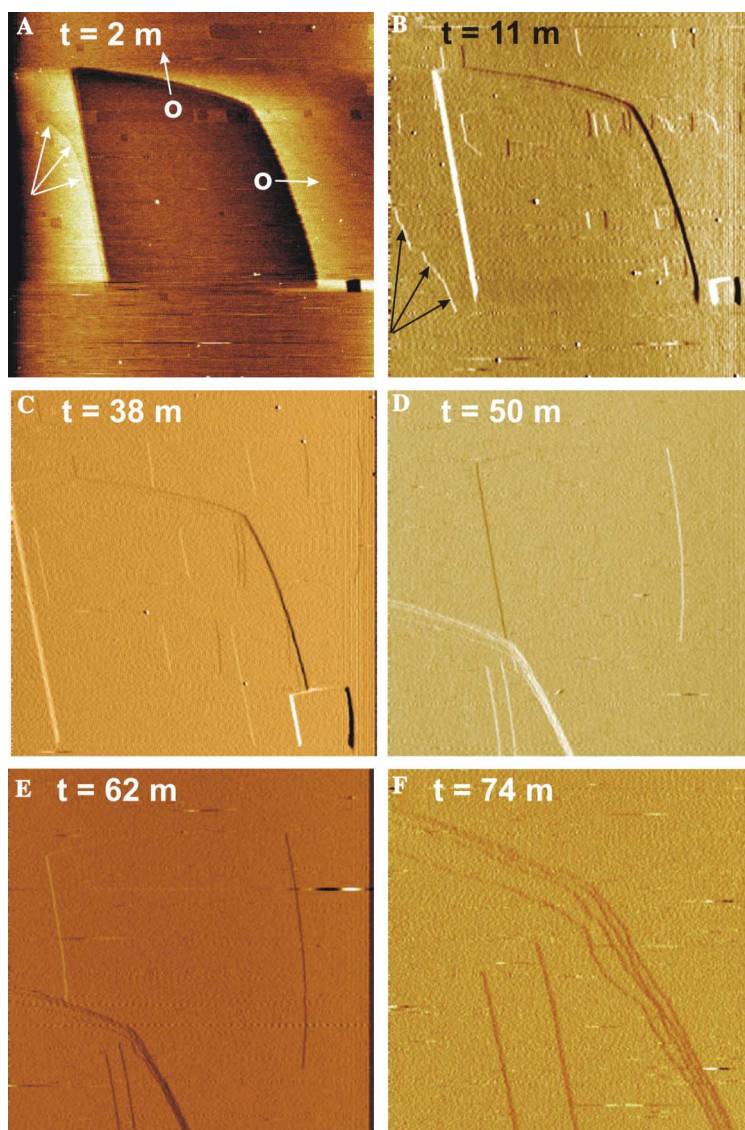

Fig. 3. Mg influence on etch pit morphology, AFM Run A4C, showing time lapse sequence immediately after introduction of 0.8×10^{-3} molal Mg to base solution. (A and B) Arrows at left indicate margin of "rough" step departing margin of large etch pit with subsequent annihilation of smaller etch pits; scan field is 10×10 µm. Motion of obtuse steps ("o→" symbols) indicated for clarity. (C) Same area after 38 minutes. (D and E) Detail of previous area, showing coalescence of small etch pit's acute steps with pinned older etch pit's obtuse steps after 50 min. Scan field is 4×4 µm. (F) 1×1 µm image detail of obtuse–obtuse corner of large older pit, contrasting ragged step edges with those of newer pit formed after Mg introduction having sharp obtuse–obtuse corner. Images (C–F) are adapted from Arvidson et al. (2004).
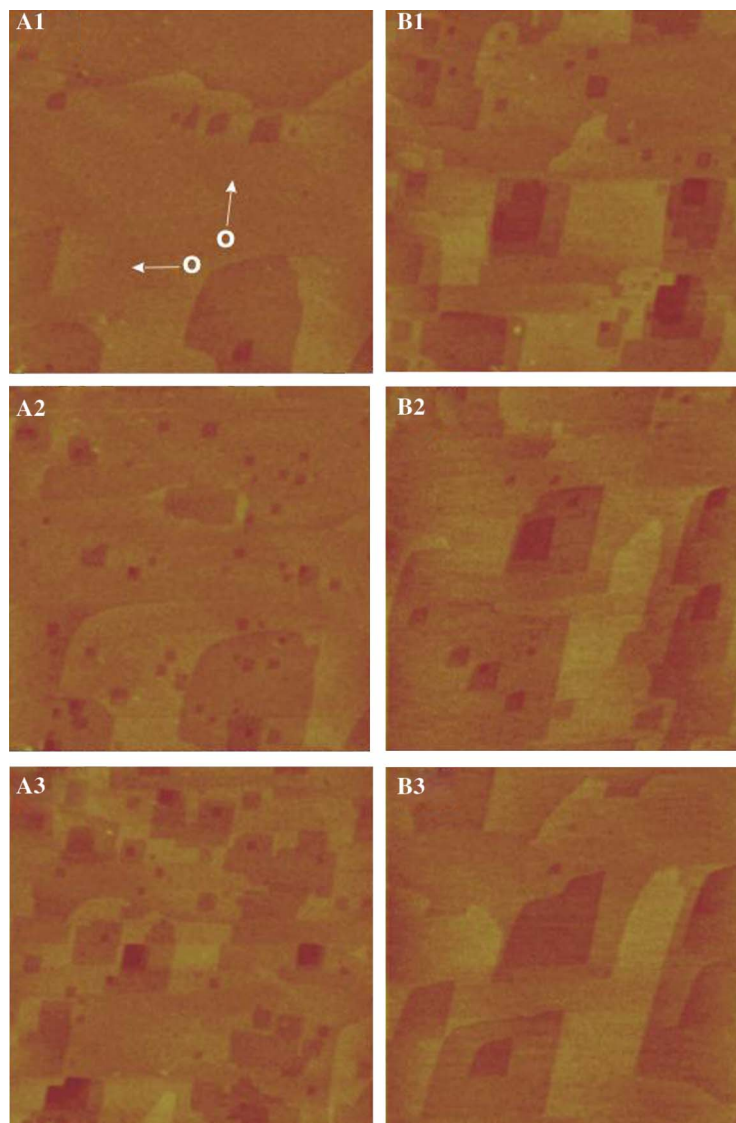
Fig. 4. Sensitivity of surface to introduction and removal of dissolved Mg in carbonated solutions, AFM Run A4C. (A1 → A3; at $t = 0$, 6, and 13 min) Time lapse sequence immediately following introduction of 0.8×10^{-3} molal Mg in base solution (4.4×10^{-3} molal NaHCO$_3$), followed by (B1 → B3; at $t = 0$, 6, and 12 min) base solution only. Arrows ("o→" symbols) indicate motion of obtuse steps for clarity; all images are 5×5 μm scans.

ment of these steps still occurs under these conditions. However, once 0.8×10^{-3} molal Mg is introduced, migration at these step edges immediately ceases. This can be seen in Fig. 3F: obtuse step edges that were in motion prior to Mg introduction reside adjacent to (newer) obtuse steps that have never been in motion.

The introduction of Mg in carbonated solutions also brought about rapid changes in etch pit density. Fig. 4 (A1–A3; Run A4C) shows the rapid emergence of numerous 0.3 nm deep etch pits immediately following introduction of magnesium. This change was not a transient artifact: new pits continued to nucleate on the surface, leading to a large increase in etch pit (and thus step) density. This effect was also reversible: the subsequent sequence (Figs. 4B1–B3) shows that magnesium's removal from the fluid cell input immediately re-establishes both the lower etch pit and step densities preceding its introduction; in

addition, movement along obtuse step edges is also re-established.

We also observed rough steps traveling at velocities substantially greater than those measured in the same field of view under the AFM (Run A4C, Figs. 3A and B). Their velocity (measured normal to the *c*-glide) was greater than 3 nm/s, much greater than the rate of straight acute steps. These rough steps appear to advance from the boundary of an etch pit (leading edge of the vicinal face), thereafter traveling rapidly over the surface, annihilating newly formed etch pits in their path, and leaving an essentially atomically flat plane in their wake. They are characterized by very high kink densities. Although they may be similar in terms of curved morphology to the pinned obtuse steps on the opposite side of the etch pit, they are clearly different in terms of velocity. These features have been described and discussed in detail in Vinson and Luttge (2005).

Lastly, we also measured step velocities as a function of dissolved inorganic carbon ($DIC \equiv CO_2 + HCO_3^- + CO_3^{2-}$) content, exchanging N_2-sparged solutions having no *carbonate* alkalinity and NaOH added to pH 8.8 (with NaCl added to maintain ionic strength), with carbonated solutions at the same pH and Mg content (0.8×10^{-3} molal, Runs A3N and A4C, Tables 1 and 2). Mean step velocities of obtuse steps were greater than acute steps (2.05 ± 0.05 versus 0.90 ± 0.09 nm/s, respectively, $v_o/v_a = 2.3 \pm 0.7$) in the CO_2-free solutions. In the carbonated solutions, acute step velocities fell only slightly (0.74 ± 0.07 nm/s), while obtuse step velocities were reduced to close to zero (0.04 ± 0.03 nm/s), giving a $v_o/v_a < 0.1$. At higher pH (Run A5N, pH 11, 0.8×10^{-3} molal Mg, DIC ~ 0), obtuse and acute AFM step velocities fell to 1.68 ± 0.09 and 0.35 ± 0.02 nm/s, respectively ($v_o/v_a = 4.8 \pm 0.4$).

4. Discussion

The fact that we record magnesium inhibition of calcite's dissolution rate is not surprising, as this effect has been described previously in the literature. Instead, our goal here is to understand how inhibition works as a surface process. Our key results are:

1. Mg added in the absence of DIC does not appear to interact strongly with the surface, even at the highest concentrations. This result is consistent with other observations at much lower pH (e.g., Alkattan et al., 2002). No variation in terms of etch pit morphology is observed at pH values between 8.8 to ~11 (oversaturated with respect to brucite, $Mg(OH)_2$, at pH > 9.9), although step velocities decrease at higher pH.

2. In the presence of DIC, the addition of sufficient Mg brings the velocity of obtuse steps essentially to zero, while acute step velocities are reduced only slightly. This is distinct from the action of carbon species alone, which generate some pinning and velocity reduction of obtuse steps, but do not arrest step motion entirely at the DIC concentrations used in these experiments (cf. Lea et al., 2001). The measured step velocities (AFM) and dissolution rates (VSI) are
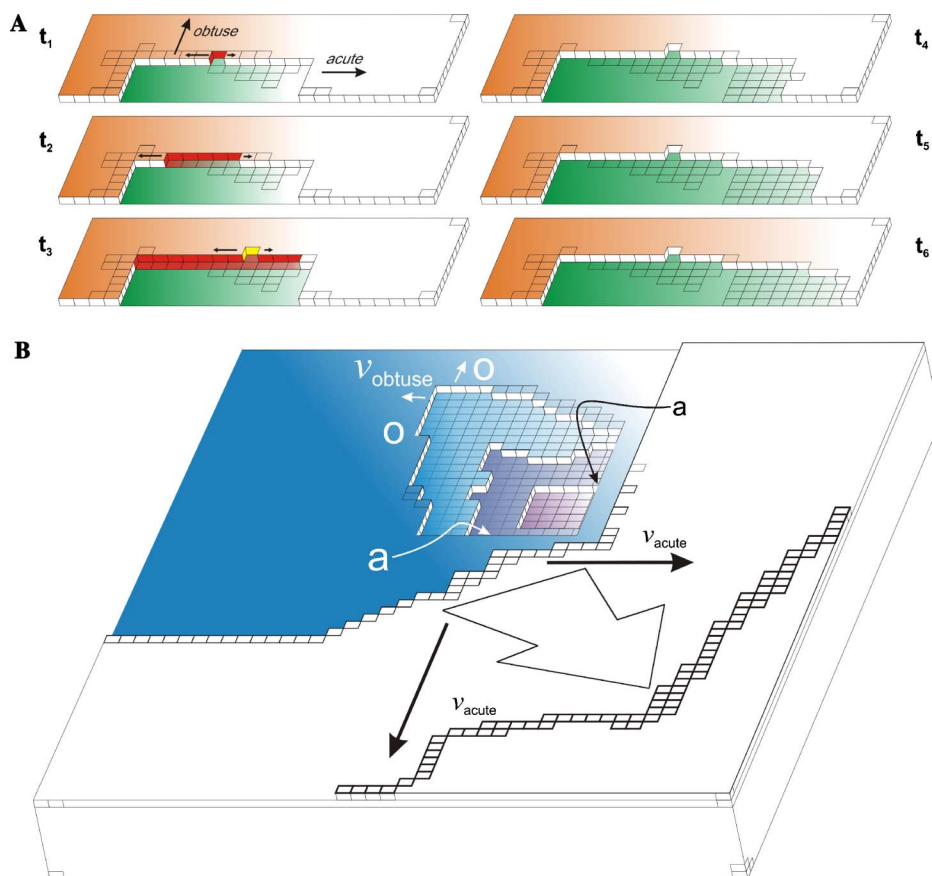

Fig. 5. Simplified schematic diagrams illustrating relationships between anisotropic kink nucleation and detachment rates and step morphology, not to scale. (A) View of obtuse and acute step edges of etch pit, with time increasing from $t_1 \rightarrow t_6$. In $t_1 \rightarrow t_3$ (Mg-free conditions), single kink detachment rate (R_K) $\gg$ double kink nucleation rate (R_{KK}) along obtuse steps, resulting in straight step morphology. In contrast, Mg (0.8×10^{-3} molal) has been introduced in $t_4 \rightarrow t_6$, resulting in subsequent inhibition of obtuse steps, and etch pit growth occurs through kink detachment along acute step only; ineffective removal of kinks along obtuse step edge results in curved morphology. (B) Summary of relationship of selective kink inhibition, step movement, overall etch pit morphology, and fast, rough steps (large arrow) in carbonated, 0.8×10^{-3} Mg solutions.

consistent with the observations of unique etch pit morphologies, maintained even after extensive dissolution. These relationships are discussed in further detail below.

3. The addition of 0.8×10^{-3} molal Mg to our carbonated base solution yields substantial increases in etch pit density (Fig. 4), and thus appears to lower the energy required for etch pit nucleation, increasing etch pit nucleation rate and effectively activating the surface. This leads to a roughening of the surface and an increase in step density, and must thus lead to an increase in surface area as well. In the same solution, we also observed the appearance of roughened, "fast" acute steps departing the margins of etch pits, with velocities several times that of "normal" (straight) acute steps. These steps are capable of annihilating newly nucleated etch pits in their path. The presence of these "upstream" pits further increases the advance rate of these steps, as the advancing "fast" step front moves instantaneously forward once upstream pits are assimilated. At the moment, we do not fully understand the relationship between the appearance of these steps and Mg concentration, or even if the two are necessarily related: Vinson and Luttge (2005) have observed their occurrence in Mg-free solutions under variable DIC concentrations.

4.1. Control of step morphology

Regardless of their magnesium content, experiments using carbonated solutions and monitored either by interferometry or the AFM record the collective or individual movement of steps that are straight (within the limits of resolution of these instruments) or curved. Step curvature can be understood in the context of a simplified terrace-ledge-kink (TLK) surface model as the outcome of two related kinetic processes: the rate of double kink nucleation (R_{KK}), and the rate of single kink detachment at obtuse–obtuse (R_{Koo}), acute–acute (R_{Kaa}), or mixed obtuse–acute (R_{Koa}, R_{Kao}) sites. The movement of kinks and kink pairs along a given step face is shown schematically in Fig. 5A. If R_{KK} is slow relative to R_K, kinks tend to annihilate one another before new kinks can form (Fig. 5A, $t_1 \rightarrow t_3$). Steps thus remain relatively straight and kink densities are low. This is the expected relationship because of differences in coordination: the energy barrier for detachment of a calcium ion at a pre-existing kink site (3 Ca–O bonds) is lower than that at a step edge. Although step movement on long steps depends on both double kink nucleation and single kink detachment, in this case average step velocity is limited by the slow nucleation rate of new double kinks (Frank, 1974; Jordan et al., 2001; Higgins et al., 2002). Liang et al. (1996) showed that straight steps and a constant step velocity require a balance between R_{KK} and the annihilation of adjacent kink pairs, with double kink nucleation rates at 0.301 and 0.129 Hz for obtuse and acute step edges under

CO$_2$-free conditions. In contrast, their rates of single kink detachment at obtuse–obtuse, acute–acute, and obtuse–acute sites (R_{Koo}, R_{Kaa}, and R_{Koa}) were much larger, at 330.6, 60.3, and 141.2 Hz, respectively.

If the single kink detachment rate, R_K, is reduced to the point where R_{KK} is competitive, then existing kinks may be preserved prior to the next cycle of kink nucleation, resulting in roughened step edges. If this situation is compounded with a pronounced difference in the velocity of one kink direction versus another, then curved step edges with high kink density are the likely result. This is the morphology often observed along obtuse step edges in Mg-free carbonated solutions, which Lea et al., 2001 attributed to carbonate ion inhibition.

In the case of Mg inhibition in carbonated solutions, the fact that we observe very little net obtuse step movement indicates that both R_{Koo} and R_{Koa} have been reduced substantially. Etch pit growth is thus controlled by kink movement along the acute step edges only (Fig. 5A, $t_4 \rightarrow t_6$). Morphologic changes in etch pits are most apparent at the highest Mg concentrations (0.8×10^{-3} molal), whereas inhibition in the rate measured by VSI occurs at Mg concentrations that are significantly lower. The most likely cause of the morphologic change is progressive inhibition of the R_{Kao} rate along the acute step edge, leading to the buildup of excess kinks at the dead obtuse step edge. In contrast, the acute step velocity is reduced in the 0.8×10^{-3} molal experiments by only ~15%. The fact that the acute steps *are* straight, not curved, also suggests that $R_K > R_{KK}$ along these step edges.

4.2. Step velocities and enhanced defect nucleation rates

Although it is possible to measure constant step velocities by the AFM in areas of etch pit formation, even in the absence of inhibition it is clear from VSI etch pit depth profiles that step velocities are not everywhere constant. Except for deep pits, most of the etch pits deeper than one monolayer consist of relatively flat floors bounded by much steeper vicinal faces forming the perimeter. Flat-bottomed pits may simply reflect a termination of the original defect. Alternatively, however, they may form if the velocity of steps radiating immediately from an interior source defect is greater than the collective motion of bounding steps composing the steep vicinal faces or "walls" of the pit.

We have confirmed this relationship by comparing the lateral expansion rates of etch pits with VSI over long time intervals (data not shown). These rates are slightly more than half the *summed* step velocities at just-formed monolayer pits recorded by the AFM. Although this problem is not resolved and is a focus of our ongoing work, we speculate that the evolution of flat-bottomed etch pits in general reflects a common process in calcite, in which a step at some point suffers a decrease in kink detachment rate. The decrease in detachment rate produces a corresponding reduction in step advance. At the perimeter of an etch pit, once the velocity of the topmost, superior steps (those farthest from the etch pit center) decrease from the maximum

velocity by Δv, the steps immediately below will arrive with a frequency proportional to $\Delta v/L(t)$, where $L(t)$ is the time-dependent terrace width separating parallel steps. An inferior step will only approach a superior one to the point where they begin to diffusively interact. This interaction in turn may reduce the inferior step's velocity; as this process continues minimum terrace widths, steep vicinal faces, and bunched steps develop, a morphology that is the essentially the rule, not the exception, in all of our observations.

The rough, fast steps described above may arise due to the coalescence of steps along $\langle 48\bar{1}\rangle_a$, $\langle \bar{4}41\rangle_a$, and thus the frequency of their appearance and their apparent velocity may depend in part on etch pit and step density. Step coalescence produces roughened, often curved, step edges with a high density of acute–acute kinks, and is also shown schematically in Fig. 5B. These steps combine high kink density with minimal inhibition (acute-obtuse, obtuse–acute, and obtuse–obtuse sites are absent or rare). Thus the high density of minimally inhibited acute–acute kink sites yields rough steps that are capable of high step velocities. Step roughening and increased kink densities have been observed during the dissolution of magnesite (Jordan et al., 2001; Higgins et al., 2002) and calcite (De Guidici, 2002) with decreasing pH under acidic conditions, and fast steps have also been noted by Jordan and Rammensee (1998). Roughened, fast steps have been observed by Vinson and Luttge (2005) in similar calcite dissolution experiments in the presence of dissolved strontium. Steps emanating from the perimeter of defect-centered etch pit are also a basic feature of the model of Lasaga and Luttge (2001). In this theoretical treatment based on a modified Gibbs–Thomson equation, dissolution is the manifest result of the coordinated movement of step chains (*stepwaves*) across the crystal surface. With sufficient undersaturation, the transit of surface stepwaves leads to a steady reduction in absolute surface height over the entire crystal surface, and thus dissolution is not limited solely to localized removal at etch pits themselves. These results mimic but are not clearly related to those achieved by Teng (2004), who observed changes in etch pit nucleation rate as a function of undersaturation, whereas *all* solutions in our experiments are highly undersaturated. This was a surprising result of these experiments, and we shall defer a complete explanation of this behavior to a future paper.

We suggest that this behavior may relate to the differences in hydration enthalpy between Mg^{2+} and Ca^{2+} ions. At the moderate pH of most of our experiments, calcite dissolution can be viewed as a hydration reaction (Sjöberg, 1978), in which the tendency for a calcium ion to detach from the surface is a function of the competition between lattice oxygen and solvent water-oxygen for the lattice cation. It is possible that magnesium interferes substantially with this process. Recent molecular dynamics and free energy calculations (Kerisit and Parker, 2004) indicate that close to the calcite surface, the hydration shells of magnesium and calcium coordinate one carbonate oxygen from the surface, with the remaining oxygens contributed by water. The hydration

shell for Ca is still incomplete, whereas magnesium is able to complete its 6-fold coordination using lattice carbonate-oxygen. There are also differences in the strength of the bond of water to a given metal cation within the first hydration shell versus that of water to the mineral surface. A water molecule may form a bond with the surface either between its oxygen and a surface calcium, or by hydrogen bonding with a surface oxygen (Kerisit and Parker, 2004). The bond between water and free calcium is weaker than that between water and surface calcium, whereas in the case of magnesium, the situation is reversed: it forms a substantially stronger bond with water, and is thus able to outcompete the surface for water of hydration. This may allow Mg to disrupt the surface hydration, favoring the formation of inner sphere over outer sphere complexes, and gives Mg a greater residence time on the calcite surface, as each water molecule also has a correspondingly longer visit in the magnesium (versus calcium) hydration shell (Kerisit and Parker, 2004).

These differences in basic behavior between Ca and Mg could support a reaction scenario in which Mg uses carbonate oxygen exposed at the calcite surface to complete its hydration shell, and upon departing is able to leave *with* the carbonate oxygen, or its surface detachment destabilizes the surface hydration layer and provides a mechanistic opportunity for subsequent detachment of lattice ions at defect sites. Mg^{2+} ion binding at *steps* clearly has a much different effect (e.g., de Leeuw, 2002), and magnesium addition in the presence of DIC evidently leads to stabilization of obtuse kinks, possibly by direct coordination in a metal kink site, a reaction step that would require more complete dehydration and provide for greater coordination on the part of the surface versus the solvent.

The latter conclusions are obviously speculative, and require support from both direct measurement and modeling. However, understanding of these effects is an important step in quantifying the role of other impurities as well. There is also a need to reconcile these direct observations of surface topography with approaches to dissolution kinetics involving surface complexation (Van Cappellen et al., 1993; Pokrovsky and Schott, 2002; Pokrovsky et al., 1999, 2005), and understand to what degree inhibition is controlled by the surface species distribution.

5. Summary and conclusions

Under specific conditions, net dissolution must reflect the cumulative result of the motion of individual steps across a crystal surface. The combination of vertical scanning interferometry and atomic force microscopy experiments yields an integrated approach to the problem of resolving how specific step motion contributes to the overall dissolution rate. Here we have used this approach to investigate how the addition of magnesium inhibits calcite dissolution in a site-specific manner.

We have documented that the addition of magnesium inhibits dissolution on calcite cleavage surfaces under far-from-equilibrium conditions in carbonated, alkaline

solutions primarily through interfering with obtuse step motion. At 0.8×10^{-3} molal Mg, obtuse step velocities are reduced to near zero and dissolution by etch pit growth proceeds via acute step movement only. Summed step velocities thus decrease from 2.95 to 0.78 nm/s, a 75% reduction. This decrease is less than the 90% reduction in dissolution rate derived from the VSI data at this same concentration. The significance of this discrepancy is still under investigation. We note, however, that the VSI data also reflect the potential changes in terrace width and step spacing (step density was not measured in the AFM data), as well as the integration of far larger portions of the mineral surface (mm^2 versus μm^2), and longer cumulative run times.

The effectiveness of Mg as an inhibitor is also a function of carbonate alkalinity, and the ratio of obtuse to acute step velocities measured in N_2-sparged solutions with no added carbon (pH 8.8, 0.8×10^{-3} molal Mg) is similar to the ratio in published AFM data for Mg-free solutions. Sufficient Mg addition results in the accumulation of excess kinks along obtuse step faces and creates unique etch pit morphologies. No evidence of epitaxial formation of a magnesium carbonate phase is seen. In contrast to the observed reduction in step velocities, etch pit nucleation rates on terraces are actually enhanced by the addition of Mg, leading to an increase in surface roughness.

Acknowledgments

Associate editor: Alfonso Mucci

References

Alkattan, M., Oelkers, E.H., Dandurand, J.-L., Schott, J., 2002. An experimental study of calcite dissolution rates at acidic conditions and 25 °C in the presence of $NaPO_3$ and $MgCl_2$. *Chemical Geology* **190**, 291–302.

Arvidson, R.S., Mackenzie, F.T., 1999. The dolomite problem: control of precipitation kinetics by temperature and saturation state. *American Journal of Science* **299**, 257–288.

Arvidson, R.S., Ertan, I.E., Amonette, J.E., Luttge, A., 2003a. Variation in calcite dissolution rates: A fundamental problem? *Geochimica et Cosmochimica Acta* **67**, 1623–1634.

Arvidson, R.S., Davis, K.J., Luttge, A., 2003b. The role of Ca^{2+}/CO_3^{2-} ratio in calcite dissolution and growth: Implications for mechanistic control of biomineralization. EOS Transactions, AGU 84(46), Fall Meeting Supplement, Abstract B12C-0793.

Arvidson, R.S., Davis, K.J., Collier, M., Amonette, J.E., Luttge, A., 2004. Etch pit morphology and magnesium inhibition of calcite dissolution. In: Wanty, R.B., Seal, R.R.P. (Eds.), *Proceedings of the 11th Symposium on Water–Rock Interactions.* Saratoga Springs/Balkema Publishers, New York, USA, pp. 721–725.

Berner, R.A., 1967. Comparative dissolution characteristics of carbonate minerals in the presence and absence of aqueous magnesium ion. *American Journal of Science* **265**, 45–70.

Berner, R.A., Morse, J.W., 1974. Dissolution kinetics of calcium carbonate in seawater. IV: Theory of calcite dissolution. *American Journal of Science* **274**, 108–134.

Berner, R.A., 1975. The role of magnesium in the crystal growth of calcite and aragonite from sea water. *Geochimica et Cosmochimica Acta* **39**, 489–504.

Blum, A.E., Lasaga, A.C., 1990. The effect of dislocation density on the dissolution rate of quartz. *Geochimica et Cosmochimica Acta* **55**, 2193–2201.

Buhmann, D., Dreybrodt, W., 1987. Calcite dissolution kinetics in the system H_2O–CO_2–$CaCO_3$ with participation of foreign ions. *Chemical Geology* **64**, 89–102.

Compton, R.G., Brown, C.A., 1994. The inhibition of calcite dissolution/precipitation: Mg^{2+} cations. *Journal of Colloid and Interface Science* **165**, 445–449.

Coles, B.A., Compton, R.G., Suárez, M., Booth, J., Hong, Q., Sanders, G.H.W., 1998. A hydrodynamic atomic force microscopy flow cell for the quantitative measurement of interfacial kinetics: The aqueous dissolution of salicylic acid and calcium carbonate. *Langmuir* **14**, 218–225.

Davis, K.J., Dove, P.M., De Yoreo, J.J., 2000. The role of Mg^{2+} as an impurity in calcite growth. *Science* **290**, 1134–1137.

Davis, K.J., Dove, P.M., De Yoreo, J.J., 2001. Resolving the control of magnesium on calcite growth: thermodynamics and kinetic consequences of impurity incorporation for biomineral formation. In: De Yoreo, J., Casey, W., Malkin, A., Vlieg, E., Ward, M. (Eds.), *Morphology and dynamics of crystal surfaces in complex molecular systems, Materials Research Society Symposium Proceedings*, vol. 620. Materials Research Society, Warrendale, PA, pp. M951–M957.

Davis, K.J., Dove, P.M., Wasylenki, L.E., De Yoreo, J.J., 2004. Morphological consequences of differential Mg^{2+} incorporation at structurally distinct steps on calcite. *American Mineralogist* **89**, 714–720.

De Guidici, G., 2002. Surface control vs. diffusion control during calcite dissolution: dependence of step-edge velocity upon solution pH. *American Mineralogist* **87**, 1279–1285.

de Leeuw, N.H., Parker, S.C., 1999. Molecular dynamics simulation of crystal dissolution from calcite steps. *Physical Review B* **60**, 13792–13799.

de Leeuw, N.H., 2002. Molecular dynamics simulations of the growth inhibiting effect of Fe^{2+}, Mg^{2+}, Cd^{2+}, and Sr^{2+} on calcite crystal growth. *Journal of Physical Chemistry B* **106**, 5241–5249.

Frank, F.C., 1974. Nucleation-controlled growth on a one-dimensional growth of finite length. *Journal of Crystal Growth* **22**, 233–236.

Gratz, A.J., Hillner, P.E., Hansma, P.K., 1993. Step dynamics and spiral growth on calcite. *Geochimica et Cosmochimica Acta* **57**, 491–495.

Gutjahr, A., Dabringhaus, H., Lacmann, R., 1996. Studies of the growth and dissolution kinetics of the $CaCO_3$ polymorphs calcite and aragonite: II. The influence of divalent cation additives on the growth and dissolution rates. *Journal of Crystal Growth* **158**, 310–315.

Higgins, S.R., Boram, L.H., Eggleston, C.M., Coles, B.A., Compton, R.G., Knauss, K.G., 2002. Dissolution kinetics, step and surface morphology of magnesite (104) in acidic aqueous solution at 60 °C by atomic force microscopy under defined hydrodynamic conditions. *Journal of Physical Chemistry B* **106**, 6696–6705.

Jordan, G., Rammensee, W., 1998. Dissolution rates of calcite obtained by scanning force microscopy: microtopography-based dissolution kinetics on surfaces with anisotropic step velocities. *Geochimica et Cosmochimica Acta* **62**, 941–947.

Jordan, G., Higgins, S.R., Eggleston, C.M., Knauss, K.G., Schmahl, W., 2001. Dissolution kinetics of magnesite in acidic aqueous solution, a hydrothermal atomic force microscopy (HAFM) study: step orientation and kink dynamics. *Geochimica et Cosmochimica Acta* **65**, 4257–4266.

Johnson, J.W., Oelkers, E.H., Helgeson, H.C., 1992. SUPCRT92: a software package for calculating the standard molal thermodynamic properties of minerals, gases, aqueous species, and reactions from 1 to 5000 bars and 0° to 1000 °C. *Computers and Geosciences* **18**, 899–947.

Kerisit, S., Parker, S.C., 2004. Free energy of adsorption of water and metal ions on the {10$\bar{1}$4}calcite surface. *Journal of the American Chemical Society* **126**, 10152–10161.

Lasaga, A.C., Luttge, A., 2001. Variation of crystal dissolution based on a dissolution stepwave model. *Science* **291**, 2400–2404.

Lea, A.S., Amonette, J.E., Baer, D.R., Liang, Y., Colton, N.G., 2001. Microscopic effects of carbonate, manganese, and strontium ions on calcite dissolution. *Geochimica et Cosmochimica Acta* **65**, 369–379.

Liang, Y., Baer, D.R., McCoy, J.M., Amonette, J.E., LaFemina, J.P., 1996. Dissolution kinetics at the calcite-water interface. *Geochimica et Cosmochimica Acta* **60**, 4883–4887.

Liang, Y., Baer, D.R., 1997. Anisotropic dissolution and CaCO$_3$ (10$\bar{1}$4)-water interface. *Surface Science* **373**, 275–287.

Luttge, A., Bolton, E.W., Lasaga, A.C., 1999. An interferometric study of the dissolution kinetics of anorthite: the role of reactive surface area. *American Journal of Science* **299**, 652–678.

Luttge, A., Winkler, U., Lasaga, A.C., 2003. An interferometric study of the dolomite dissolution: a new conceptual model for mineral dissolution. *Geochimica et Cosmochimica Acta* **67**, 1099–1116.

MacInnis, I.N., Brantley, S.L., 1993. Development of etch pit size distributions on dissolving minerals. *Chemical Geology* **105**, 1–49.

Morse, J.W., 1974. Dissolution kinetics of calcium carbonate in sea water. V: effects of natural inhibitors and the position of the chemical lysocline. *American Journal of Science* **274**, 638–647.

Paquette, J., Reeder, R.J., 1995. Relationship between surface structure, growth mechanism, and trace element incorporation in calcite. *Geochimica et Cosmochimica Acta* **59**, 735–749.

Pokrovsky, O.S., Schott, J., Thomas, F., 1999. Processes at the magnesium bearing carbonates/solution interface. I.A surface speciation model for magnesite. *Geochimica et Cosmochimica Acta* **63**, 863–880.

Pokrovsky, O.S., Schott, J., 2002. Surface chemistry and dissolution kinetics of divalent metal carbonates. *Environmental Science & Technology* **36**, 426–432.

Pokrovsky, O.S., Golubev, S.V., Schott, J., 2005. Dissolution kinetics of calcite, dolomite and magnesite at 25 °C and 0 to 50 atm pCO$_2$. *Chemical Geology* **217**, 239–255.

Sabbides, G., Koutsoukos, P.G., 1995. Dissolution of calcite carbonate in the presence of magnesium and orthophosphate. In: Amjad, Z. (Ed.), *Mineral Scale Formation and Inhibition*. Plenum Press, New York, pp. 73–86.

Sjöberg, E.L., 1978. Kinetics and mechanism of calcite dissolution in aqueous solutions at low temperatures. *Stockholm Contributions in Geology* **32**, 92.

Teng, H.H., Dove, P.M., Orme, C.A., De Yoreo, J.J., 1998. Thermodynamics of calcite growth: baseline for understanding biomineral formation. *Science* **282**, 724–727.

Teng, H.H., Dove, P.M., De Yoreo, J.J., 1999. Reversed calcium carbonate morphologies induced by controlling microscopic growth kinetics: insight into biomineralization. *Geochimica et Cosmochimica Acta* **63**, 2507–2512.

Teng, H.H., 2004. Controls by saturation state on etch pit formation during calcite dissolution. *Geochimica et Cosmochimica Acta* **68**, 253–262.

Van Cappellen, P., Charlet, L., Stumm, W., Wersin, P., 1993. A surface complexation model of the carbonate mineral-aqueous solution interface. *Geochimica et Cosmochimica Acta* **57**, 3505–3518.

Vinson, M.D., Luttge, A., 2005. Multiple length-scale kinetics: an integrated study of calcite dissolution rates and strontium inhibition. *American Journal of Science* **305**, 119–146.

Wasylenki, L.E., Dove, P.M., De Yoreo, J.J., 2004. Direct measurement of Mg partitioning into calcite as a function of temperature, growth rate, and solution chemistry: quantification of inorganic controls on the Mg/Ca paleothermometer. *Geochimica et Cosmochimica Acta* **69**, 3017–3027.